GEOPHYSICS, VOL. 70, NO. 4 (JULY-AUGUST 2005); P. R15–R23, 9 FIGS., 1 TABLE.
10.1190/1.1990220

Subsonic near-surface P-velocity and low S-velocity observations using propagator inversion

Robbert van Vossen[1], Andrew Curtis[2], and Jeannot Trampert[1]

ABSTRACT

Detailed knowledge of near-surface P- and S-wave velocities is important for processing and interpreting multicomponent land seismic data because (1) the entire wavefield passes through and is influenced by the near-surface soil conditions, (2) both source repeatability and receiver coupling also depend on these conditions, and (3) near-surface P- and S-wave velocities are required for wavefield decomposition and demultiple methods. However, it is often difficult to measure these velocities with conventional techniques because sensitivity to shallow-wave velocities is low and because of the presence of sharp velocity contrasts or gradients close to the earth's free surface. We demonstrate that these near-surface P- and S-wave velocities can be obtained using a propagator inversion. This approach requires data recorded by at least one multicomponent geophone at the surface and an additional multicomponent geophone at depth. The propagator between them then contains all information on the medium parameters governing wave propagation between the geophones at the surface and at depth. Hence, inverting the propagator gives local estimates for these parameters. This technique has been applied to data acquired in Zeist, the Netherlands. The near-surface sediments at this site are unconsolidated sands with a thin vegetation soil on top, and the sediments considered are located above the groundwater table. A buried geophone was positioned 1.05 m beneath receivers on the surface. Propagator inversion yielded low near-surface velocities, namely, 270 ± 15 m/s for the compressional-wave velocity, which is well below the sound velocity in air, and 150 ± 9 m/s for the shear velocity. Existing methods designed for imaging deeper structures cannot resolve these shallow material properties. Furthermore, velocities usually increase rapidly with depth close to the earth's surface because of increasing confining pressure. We suspect that for this reason, subsonic near-surface P-wave velocities are not commonly observed.

INTRODUCTION

Strong near-surface velocity contrasts are often encountered in land seismic surveys. Both P- and S-wave velocities may increase by nearly an order of magnitude at the interface defining the top of the bedrock, and P-velocities increase up to 100% across the top depth of total water saturation (Stümpel et al., 1984; Goforth and Hayward, 1992).

Detailed knowledge of near-surface velocities is essential for engineering applications and groundwater and environmental projects (Ward, 1990). Furthermore, this knowledge is required to correctly process and interpret (multicomponent) land data. For instance, near-surface soil conditions have a significant influence on source wavelet and radiation patterns (Kähler and Meissner, 1983; Aritman, 2001). Also, wavefield decomposition, which enables independent interpretation of up- and downgoing P- and S-waves, requires the free-surface reflectivity to be known accurately (e.g., Dankbaar, 1985; Wapenaar et al., 1990; Robertsson and Curtis, 2002). Wavefield decomposition is a prerequisite for demultiple methods (Verschuur et al., 1992), which are especially important in media with a near-surface low-velocity layer that may act as a wave guide in which energy may propagate over long distances with little loss from geometric spreading. This could mask reflections from a deeper target (Hunter et al., 1984; Robertsson et al., 1996). Demultiple methods remove these guided waves.

While shallow material properties are especially important for processing and interpretation of multicomponent seismic data, near-surface wave velocities usually cannot be resolved

Presented at the 73rd International Meeting, SEG, 2003. Manuscript received by the Editor October 21, 2003; revised manuscript received December 17, 2004; published online July 7, 2005.
[1]Utrecht University, Department of Earth Sciences, Budapestlaan 4, 3584 CD Utrecht, the Netherlands. E-mail: vossen@geo.uu.nl; trampert@geo.uu.nl.
[2]Schlumberger Cambridge Research, High Cross, Madingley Road, Cambridge CB3 0EL, United Kingdom; and The University of Edinburgh, School of GeoSciences, Grant Institute, West Mains Road, Edinburgh, EH9 3JW, Scotland. E-mail: curtis@cambridge.oilfield.slb.com.

with an acquisition geometry designed for imaging deeper structure. Detailed information can, however, be obtained with shallow, high-resolution reflection and refraction experiments (Doornenbal and Helbig, 1983; Hunter et al., 1984; Steeples and Miller, 1990). These techniques use arrays of closely spaced geophones and high frequencies to obtain detailed images of the shallow subsurface.

Subsonic P-wave velocities have been observed with these shallow, high-resolution seismic experiments by analyzing moveout velocities close to the source (Birkelo et al., 1987; Bachrach and Nur, 1998; Bachrach et al., 1998; Baker et al., 1999), whereas they are not commonly observed using conventional seismic techniques. This is a consequence of the different depth sensitivities of these methods, combined with a near-surface velocity gradient caused by increasing confining pressure. A drawback of estimating near-source moveout velocities is that the complexity of the near-source field requires careful processing and interpretation of these types of data to avoid misinterpretation of recorded events (Michaels, 2002).

Recently, Curtis and Robertsson (2002) introduced a technique for estimating local near-surface velocities using a 3D geophone configuration. Geophones are not only deployed at the surface but also at shallow depths to enhance imaging of the near-surface without having to perform an additional high-resolution experiment. With the proposed 3D geophone configuration, spatial wavefield derivatives can be approximated, allowing inversion of the wave equation for near-surface P- and S-wave velocities (Curtis and Robertsson, 2002). An advantage of this method is its applicability to the complete wavefield; a drawback is its sensitivity to deployment-related errors (Muijs et al., 2002).

We present results from a technique referred to as propagator inversion (PI) (Trampert et al., 1993; Van Vossen et al., 2004). This technique also uses a 3D geophone configuration to determine near-surface P- and S-wave velocities, but it avoids explicit computation of spatial wavefield derivatives and is therefore less sensitive to deployment-related errors. Moreover, it does not require measurement and interpretation of moveout velocities in the near-source region, and it can be incorporated in a seismic survey for imaging deeper structure without having to perform an additional high-resolution experiment.

PROPAGATOR ESTIMATION FROM DATA

Propagator matrices were introduced in seismology by Thomson (1950) and Haskell (1953) and generalized by Gilbert and Backus (1965). These matrices describe the propagation of plane waves through a horizontally layered medium. Throughout this paper, the free surface is used as a reference level. The propagator can then be interpreted as a wavefield-extrapolation filter. Application of the propagator to the recorded wavefield at the free surface gives the wavefield at depth Δz.

Trampert et al. (1993) introduced SH PI to obtain the SH-wave velocity structure and the quality factor in a borehole. This propagator can be obtained from the recorded data by taking the spectral ratio of a downhole record over a surface record. It is completely determined by the medium parameters governing wavefield propagation between these two records. Recently, Van Vossen et al. (2004) formulated propagator estimation for the elastic P-SV case. We briefly review this concept before we discuss the inversion scheme for near-surface material parameters.

In an isotropic medium, the propagator naturally decomposes into SH and coupled P-SV waves. The anelastic SH case is fully treated by Trampert et al. (1993) We only review the elastic P-SV case here. Denote the inline particle-velocity component by v_1 and the vertical component by v_3. The full propagator is a 4×4 matrix, and the boundary conditions state that the free surface is stress free, so that the wavefield at depth Δz is related to the wavefield recorded at the free surface ($z = 0$) by:

$$\begin{pmatrix} v_1(\omega, x, \Delta z) \\ v_3(\omega, x, \Delta z) \end{pmatrix} = \begin{pmatrix} P_{11} & P_{13} \\ P_{31} & P_{33} \end{pmatrix} \begin{pmatrix} v_1(\omega, x, 0) \\ v_3(\omega, x, 0) \end{pmatrix}. \quad (1)$$

For an elastic, homogeneous medium, with P velocity α and S velocity β, the propagator coefficients read in the time domain (Aki and Richards, 2002; Van Vossen et al., 2004) as

$$P_{11} = \beta^2 p^2 G_1^P + [(1 - 2\beta^2 p^2)/2] G_1^S, \quad (2)$$

$$P_{33} = [(1 - 2\beta^2 p^2)/2] G_1^P + \beta^2 p^2 G_1^S, \quad (3)$$

$$P_{13} = \left[p(1 - 2\beta^2 p^2)/(2q_P)\right] G_2^P - \beta^2 p q_S G_2^S, \quad (4)$$

$$P_{31} = \beta^2 p q_P G_2^P - \left[p(1 - 2\beta^2 p^2)/(2q_s)\right] G_2^S, \quad (5)$$

where

$$G_1^P = \delta(t + q_P \Delta z) + \delta(t - q_P \Delta z), \quad (6)$$

$$G_2^P = \delta(t + q_P \Delta z) - \delta(t - q_P \Delta z), \quad (7)$$

$$G_1^S = \delta(t + q_S \Delta z) + \delta(t - q_S \Delta z), \quad (8)$$

$$G_2^S = \delta(t + q_S \Delta z) - \delta(t - q_S \Delta z). \quad (9)$$

The horizontal slowness is denoted by p, and the vertical slownesses q_P and q_S are

$$q_P = (\alpha^{-2} - p^2)^{1/2}, \quad (10)$$

$$q_S = (\beta^{-2} - p^2)^{1/2}. \quad (11)$$

These theoretical expressions show that P_{11} and P_{33} are symmetric around $t = 0$, whereas P_{13} and P_{31} are antisymmetric around $t = 0$. Thus, in the frequency domain, P_{11} and P_{33} are entirely real, and P_{13} and P_{31} are purely imaginary. As a result, we can directly estimate the components of $P_{ij}(\omega)$ by equating real and imaginary parts in equation 1. In the following, we denote the propagator coefficients estimated from the data with $\tilde{\mathbf{P}}(\omega)$. The explicit expressions for estimating $\tilde{\mathbf{P}}(\omega)$ are

$$\tilde{P}_{11} = \{\Re[v_3(\omega, 0)]\Re[v_1(\omega, \Delta z)] + \Im[v_3(\omega, 0)]\Im[v_1(\omega, \Delta z)]\}/D(\omega), \quad (12)$$

$$\tilde{P}_{33} = \{\Re[v_1(\omega, 0)]\Re[v_3(\omega, \Delta z)] + \Im[v_1(\omega, 0)]\Im[v_3(\omega, \Delta z)]\}/D(\omega), \quad (13)$$

$$\tilde{P}_{13} = i\{\Re[v_1(\omega, 0)]\Im[v_1(\omega, \Delta z)] - \Im[v_1(\omega, 0)]\Re[v_1(\omega, \Delta z)]\}/D(\omega), \quad (14)$$

$$\tilde{P}_{31} = i\{\Re[v_3(\omega, 0)]\Im[v_3(\omega, \Delta z)] - \Im[v_3(\omega, 0)]\Re[v_3(\omega, \Delta z)]\}/D(\omega), \quad (15)$$

with the denominator $D(\omega)$ given by

$$D(\omega) = \Re[v_3(\omega, 0)]\Re[v_1(\omega, 0)] + \Im[v_3(\omega, 0)]\Im[v_1(\omega, 0)]. \quad (16)$$

In these equations, $\Re[v_1(\omega, \Delta z)]$ is the real part of $v_1(\omega, \Delta z)$, $\Im[v_1(\omega, \Delta z)]$ is the imaginary part, and i denotes the imaginary unit $\sqrt{-1}$. Note that the symmetry properties used to obtain explicit expressions for the propagator filters break down in the viscoelastic case. Then, only the SH propagator can be directly obtained from the data (Trampert et al., 1993).

Van Vossen et al. (2004) computed $\tilde{\mathbf{P}}$ with a stabilized spectral division using the so-called water-level method (Helmberger and Wiggins, 1971). Stabilization is required because of a limited bandwidth of $D(\omega)$, and interfering waves may introduce internal notches in $D(\omega)$. However, a problem associated with this method is that the amount of stabilization can influence the estimates for the propagator (Ammon, 1991), which may affect the inversion results as well (Van Vossen et al., 2004). To avoid these problems, we decided instead to implement the spectral divisions in the time domain using a Wiener deconvolution scheme. Either symmetric ($\tilde{P}_{11}$ and $\tilde{P}_{33}$) or antisymmetric filters ($\tilde{P}_{13}$ and $\tilde{P}_{31}$) around $t = 0$ are constructed with N independent coefficients. Details on the implementation of the acausal Wiener deconvolution can be found in Appendix A.

PROPAGATOR INVERSION (PI)

In the previous section, we showed that $\tilde{\mathbf{P}}$ can be obtained from data recorded by one surface geophone and one at depth. In this section, we outline the inverse procedure for estimating the near-surface velocities α and β from $\tilde{\mathbf{P}}$.

A flow diagram for the inverse problem is shown in Figure 1. The 3D receiver configuration used for the Zeist field experiment in the Netherlands, conducted to test propagator estimation and inversion, is shown in Figure 2. We discuss this experiment in detail in the next section. The configuration has multicomponent geophones positioned in a cross shape at the surface. Two geophones are buried at the center of the receiving group. Strictly speaking, propagator estimation requires only one multicomponent geophone positioned at the surface and a second geophone at depth. Then, the horizontal slowness also needs to be constrained by the inverse procedure.

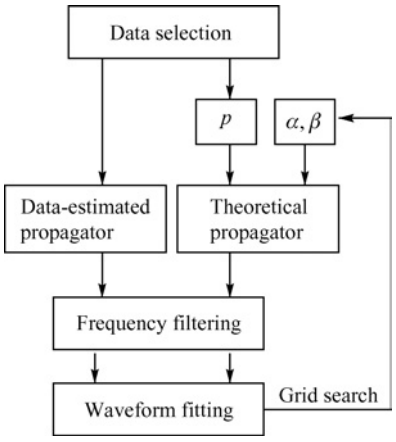

Figure 1. Propagator inversion scheme for α and β.

However, we do not have to incorporate horizontal slowness in the inverse procedure when a short array of geophones is deployed at the surface, since it can be measured directly.

PI consists of the following steps. First, a data window is selected to isolate an arrival. The window is tapered at its edges by a cosine taper. Second, the selected data are used as input for propagator estimation. The horizontal slowness p of the dominant arrival in this time window can be determined using the array of geophones in the inline direction x. This is accomplished by estimating the time shifts for which the stack power is optimized. The remaining unknown parameters in the theoretical propagator for a homogeneous isotropic medium are α and β (equations 2–11). Values for α and β are selected using a grid-search technique. A physical bound is imposed such that $\beta < \alpha/\sqrt{2}$, i.e., the Poisson's ratio has to be positive. Given values for α, β, and p, the theoretical propagator can be evaluated. Before comparing the waveforms of the theoretical propagator $\mathbf{P}$ to the data-estimated propagator $\tilde{\mathbf{P}}$, frequency filtering is necessary since $\tilde{\mathbf{P}}$ is band-limited, whereas $\mathbf{P}$ has an infinite bandwidth. After bandwidth equalization, the propagator waveforms can be compared to each other. The L2 norm was used as the objective function:

$$E_{ij} = \left\{ \sum_{t=-N\Delta t}^{N\Delta t} \left[\tilde{P}_{ij}(t) - P_{ij}(t, \alpha, \beta, p)\right]^2 \right\}^{1/2}, \quad (17)$$

with $i, j = 1, 3$. The objective function for the joint inverse of all propagator coefficients is given by the sum of all individual misfit functions,

$$E_{tot} = E_{11} + E_{13} + E_{31} + E_{33}. \quad (18)$$

Estimates for α and β can be obtained by minimizing E_{tot}.

APPLICATION ON ZEIST FIELD DATA

We illustrate PI on a field data set acquired in Zeist, the Netherlands. On this site, the near-surface material mainly consists of unconsolidated sands, with a thin layer of vegetal soil on top.

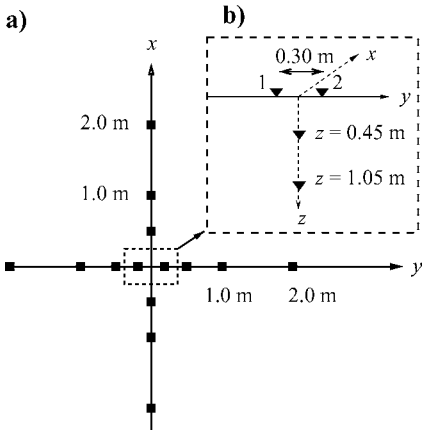

Figure 2. 3D receiver configuration for the Zeist field experiment, (a) top view and (b) front view. All geophones were multicomponent geophones, and the source positions were located on the x-axis.

Data acquisition

A walkaway noise test was performed with 3C 4.5-Hz geophones at offsets between 0.75 and 84 m, with 0.75-m geophone spacing. These data (Figure 3) show that ground roll and guided waves are dominant in the recordings. In addition, measurements were made with a dense 3D 3C receiving configuration that will be used for PI (see Figure 2). Geophones were positioned in a cross shape at the surface. In the x-direction, receivers were located at 0.50, 1.00, and 2.00 m distance to the center of the configuration; in the y-direction, the distances were 0.15, 0.50, 1.00, and 2.00 m. The buried geophones were positioned at 0.45 and 1.05 m depth, respectively. Geophones can be buried efficiently in unconsolidated sediments using a hand ground drill. This approach minimizes the medium perturbations caused by burial of geophones. For the dense 3D 3C group, data were acquired using 11 different source positions located between 35- and 85-m offset. The shot spacing was 5.0 m, and all shot points were located on the x-axis. The experiment was repeated four times for every shot position. During the whole experiment, a weight drop was used; a steel ball of about 37 kg was dropped from approximately 3.5 m height on a steel plate resting on the ground. The recording instrument was a Bison Spectra with 48 channels, and the time-sampling interval was 0.25 ms.

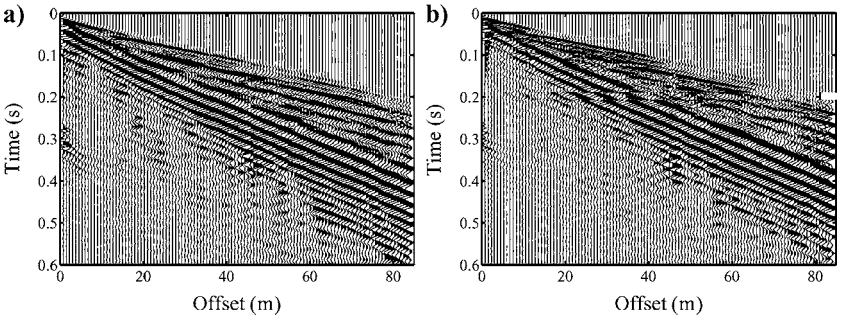

Figure 3. Walkaway noise survey for (a) v_x and (b) v_z. The panels are displayed with trace normalization.

Table 1. Horizontal slowness estimates for each shot position. Data are selected in time windows with t between t_1 and t_2.

Shot number	Offset (m)	t_1 (s)	t_2 (s)	p (ms/m)	$\sigma(p)$ (ms/m)
1	85	0.19	0.26	2.10	0.11
2	80	0.18	0.25	2.12	0.07
3	75	0.17	0.24	2.23	0.03
4	70	0.16	0.23	2.18	0.06
5	65	0.15	0.22	2.20	0.06
6	60	0.14	0.21	2.15	0.06
7	55	0.13	0.20	2.12	0.04
8	50	0.11	0.18	2.11	0.03
9	45	0.09	0.17	2.23	0.05
10	40	0.08	0.16	2.19	0.05
11	35	0.07	0.14	2.21	0.03
Mean				2.17	0.05

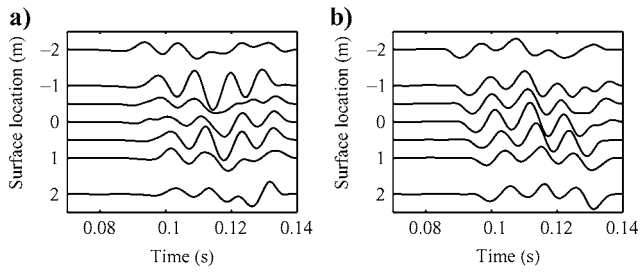

Figure 4. (a) Inline- and (b) vertical-component recordings with the source located at 35 m distance to the center of the receiver group.

Data selection and estimation of horizontal slowness

In theory, the propagator method is valid for a single slowness, i.e., isolating an arrival as uncontaminated as possible by other arrivals. On the other hand, considering only very short time windows results in a poor signal-to-noise ratio. Synthetic experiments demonstrate that PI is insensitive to small slowness variations in the selected data (Van Vossen et al., 2004). Therefore, we selected data windows including all events arriving before the ground roll. For each shot position, time windows that contain the selected data are listed in Table 1. A cosine taper with 0.01 s length was applied to both edges of the window. An example of data selected for slowness estimation is shown in Figure 4. A bandpass filter with cut-off frequencies between 40 and 140 Hz was applied to these recordings. The events shown may be interpreted as trapped waves above the groundwater table. Because there are significant differences in the recorded amplitudes on the inline component, we decided to estimate p using only the vertical component of the recorded particle velocity. These slowness estimates are given for each shot position in Table 1. The differences between the estimated horizontal slownesses for the different source positions are small.

Propagator estimation and inversion

Contrary to horizontal-slowness estimation, no frequency filtering was applied to the selected data prior to propagator estimation. An example of the data used for propagator estimation is shown in Figure 5. It shows that recordings rapidly change with depth, especially on the vertical component. At 0.45 m depth, high frequencies are strongly attenuated compared to the recordings obtained at the free surface and at 1.05 m depth. On the other hand, the low-frequency content of the signal decays with depth. This characteristic behavior is caused by interference between the free-surface incident wave and its reflected and converted waves.

Interpretation of the data recorded on the horizontal component is difficult. The two surface geophones show significant amplitude differences in the high-frequency part of the spectrum. For lower frequencies, on the other hand, there is excellent agreement between these recordings. This observation could indicate coupling differences between these two surface geophones (Krohn, 1984). Another interesting observation is that the amount of energy recorded in the 50- to 60-Hz frequency band is small, although we did not apply a notch filter to the data.

We demonstrate PI first using surface geophone 1 and the buried geophone at 1.05 m depth. Then, we consider the data recorded by surface geophone 2. Given the frequency content of the signal and the time-sampling interval of 0.25 ms, accurate velocity estimation with the geophone buried at 0.45 m depth is, in our opinion, not feasible.

Figure 6 shows the data-estimated propagator for each shot position. The frequency passband is between 40 and 140 Hz. The theoretical propagator **P** is shown with α and β for which E_{tot} is minimized. There is good agreement between $\tilde{\mathbf{P}}$ and **P** for most individual shots. Since the changes in the estimated horizontal slowness are small (Table 1), stacking of the data-estimated propagator components over all source positions is not in conflict with the single slowness assumption. This process enhances the signal-to-noise ratio of the data-estimated propagator. Figure 6 shows that an excellent fit is obtained between the averaged propagator components and the best-fitting theoretical propagator.

The constraints offered by each individual propagator component are shown in Figure 7a-d. Misfit functions are shown for the stacked propagator, and the minima of the prestack propagators illustrate the uncertainty. No computations are performed with combinations for α and β for which the Poisson's ratio becomes negative. The misfit functions show that P_{11} and P_{31} are dominantly sensitive to variations in β, whereas P_{33} is more sensitive to variations in α. P_{13} contains information on both α and β. Because P_{33} is dominantly sensitive to variations in α, $(\beta p)^2 \ll 1$ (equation 3). This is confirmed by Table 1. Thus, for near-vertical incident waves, the PI is dominantly sensitive to phase differences rather than amplitude effects as a result of interaction of the incident wavefield with the free surface. However, close to the critical angle for incident S-waves, the amplitude coefficient of P_{13} changes rapidly, which results in sensitivity for both α and β.

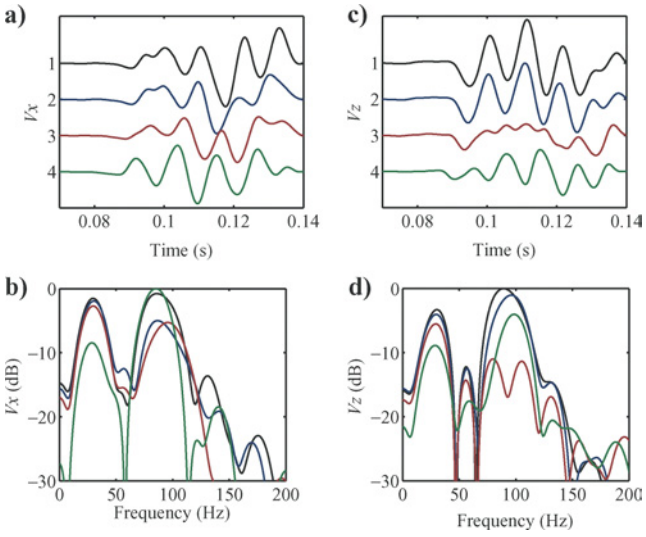

Figure 5. Traces and amplitude spectra for v_x (a, b) and for v_z (c, d) for different depths, recorded at 35-m offset. The black and blue traces are the recordings acquired at the free surface by the geophones labeled 1 and 2 (Figure 2); the red traces were acquired at 0.45 m depth and the green traces at 1.05 m depth.

Figure 7e illustrates the joint inversion for all propagator coefficients. Both α and β are well constrained. The minimum of the joint inversion is equal to the average of all minima of the misfit functions for each individual shot. We obtain the following estimates: $\alpha = 270 \pm 15$ m/s and $\beta = 150 \pm 9$ m/s. The uncertainties given are the standard deviations of the variation of best estimates for the individual shots.

So far we have only discussed the data-estimated propagator obtained using surface geophone 1. Because there are significant differences between the horizontal component recordings 1 and 2 (Figure 5), it is important to assess the consequences of these data differences on propagator estimation and inversion. This allows us to determine whether PI is robust in the presence of realistic data errors. Figure 8 shows that the match between $\tilde{\mathbf{P}}$ and **P** is not as good compared to the results for surface geophone 1, although the fit is good for the first three shot points and for P_{33}. This propagator coefficient is not significantly affected by data variations on the horizontal component: it relates the vertical component acquired at the free surface to the same component at depth (equation 1). The high-cut frequency was lowered to 100 Hz to reduce the

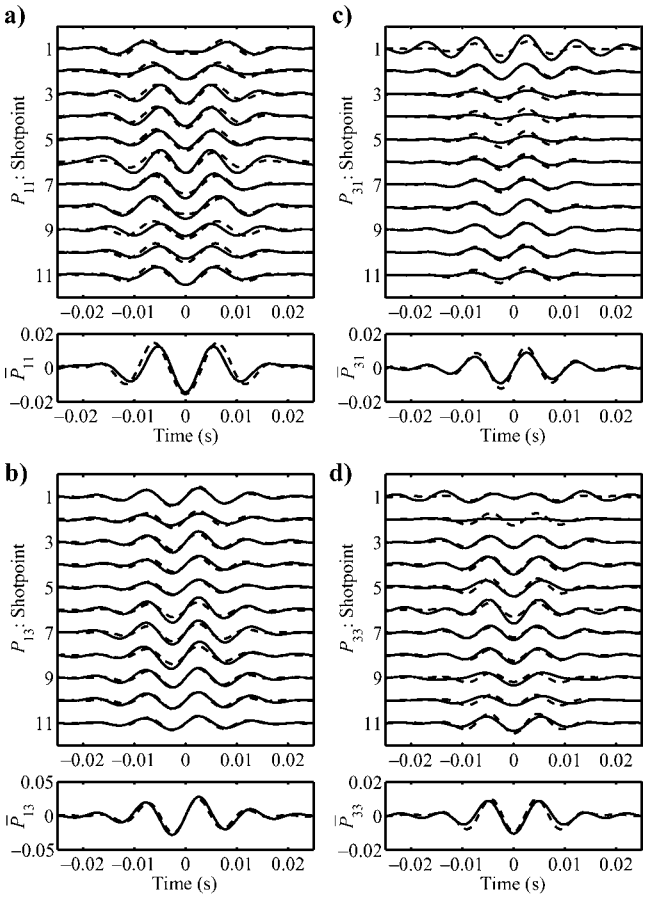

Figure 6. Individual and averaged (stacked) data-estimated propagators (solid) compared to the best fitting theoretical propagator (dashed). Shown are (a) P_{11}, (b) P_{13}, (c) P_{31}, and (d) P_{33}. The data-estimated propagators are computed using surface geophone 1 and the buried geophone at 1.05 m depth. Frequency filters are applied with a passband between 40 and 140 Hz.

effects of coupling errors to the velocity estimation. The misfit function for the joint inverse of all stacked propagators is shown in Figure 7f. The velocities corresponding to the minimum of E_{tot} are $\alpha = 230$ m/s and $\beta = 155$ m/s. Averaging all individual shots gives $\alpha = 244 \pm 20$ m/s and $\beta = 152 \pm 14$ m/s. The estimates for β agree well with the previously obtained velocity estimates, whereas α is less consistent. For shotpoints 1, 2, and 3, which show a good match between $\tilde{\mathbf{P}}$ and $\mathbf{P}$, we find that $\alpha \geq 260$ m/s.

Although geophones 1 and 2 were close together (0.30 m between them), the horizontal-component data recorded by these two geophones significantly differ for frequencies above 70 Hz. These amplitude differences are attributed to geophone-ground coupling. This refers to the accuracy with which a geophone measures the actual ground motion. It is especially relevant for horizontal-component recordings. A well-coupled horizontal geophone has a coupling-resonance frequency of 130 Hz, whereas poorly coupled horizontal geophones could have significantly lower (down to 30 Hz) resonance frequencies (Krohn 1984). For frequencies much lower than the coupling-resonance frequency, the geophone accurately follows the ground motion.

The results of surface geophone 1 are not sensitive to changes in the high-cut frequency from 100 up to 140 Hz. Increasing this frequency reduces the uncertainty in the velocity estimates. For surface geophone 2, on the other hand, increasing this frequency resulted in poor fits of the propagator coefficients and large uncertainties in the estimated velocities. Therefore, we decided to use different frequency bands for the application of PI to data acquired by surface geophones 1 and 2. The obtained results are barely influenced by the choice of the low-cut frequency. Lowering this frequency to 20 Hz yielded similar velocity estimates, although the data misfit between $\mathbf{P}$ and $\tilde{\mathbf{P}}$ increased somewhat, resulting in larger uncertainties attached to these estimates. Therefore, we selected 40 Hz as the low-cut frequency.

Thus, the analysis indicates that best results are obtained with the data recorded by surface geophone 1: inversion results are stable up to 140 Hz, a better data fit is obtained, and the data have a better resolving power for near-surface P- and S-wave velocities. Although the data quality of the recordings of surface geophone 2 is poorer, the estimate for the S-wave velocity is in agreement with the results obtained with surface geophone 1, and the difference between the obtained P-wave velocities is approximately 10% of the estimated value. This

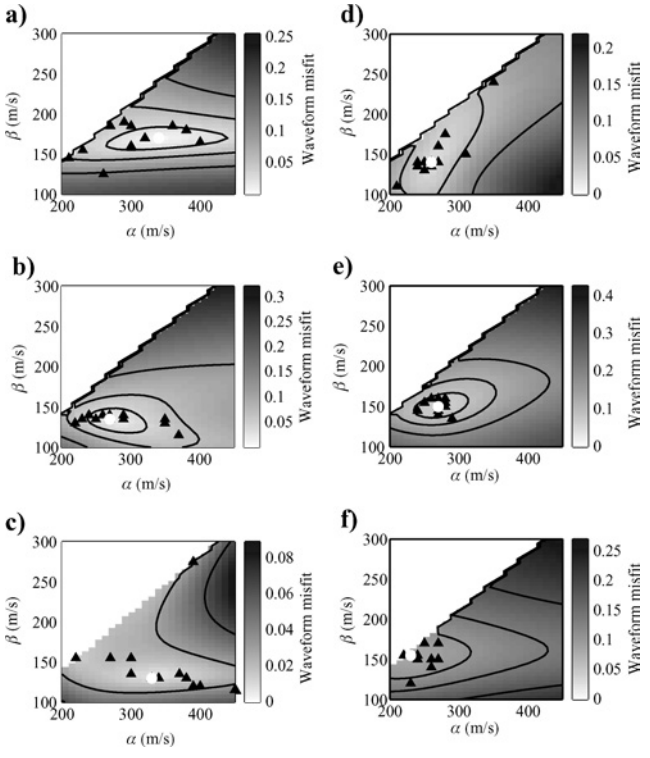

Figure 7. Waveform misfit functions (a) E_{11}, (b) E_{13}, (c) E_{31}, (d) E_{33} for poststack P_{11}, P_{13}, P_{31}, and P_{33} computed using surface geophone 1. The combined constraints are shown in (e). The joint inverse results using surface geophone 2 are shown in (f). Contours are drawn for $E_{ij} = min(E_{ij}) + c$, with $c = 0.02$, 0.05, and 0.10, and the indices i and j take the values 1 or 3. The open circle denotes the minimum of E_{ij}, and the triangles indicate the positions of the minima of E_{ij} for each individual shot. No computations are performed in the nonphysical region $\beta > \alpha/\sqrt{2}$.

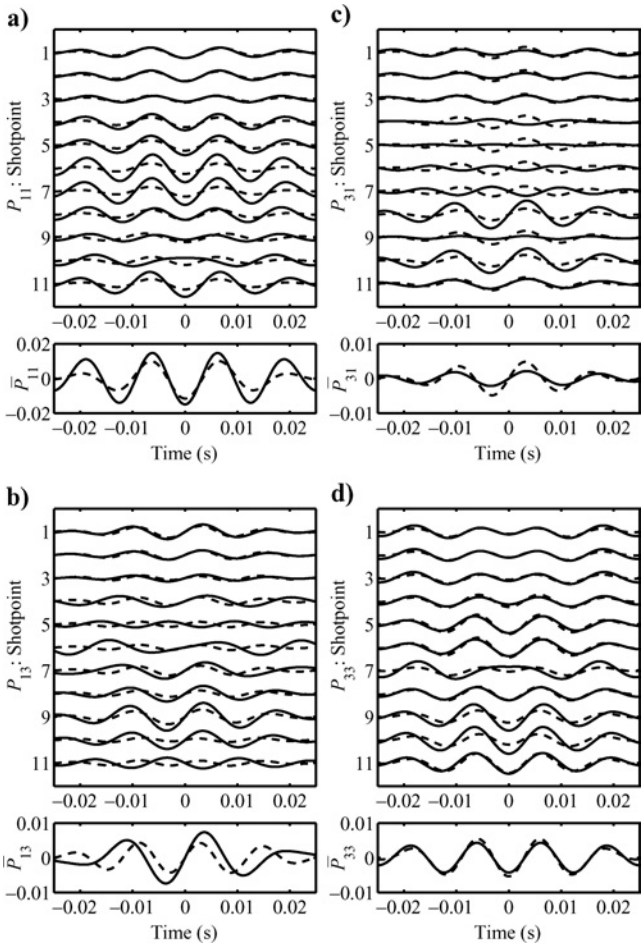

Figure 8. Individual and averaged data-estimated propagators (solid) compared to the best-fitting theoretical propagator (dashed). Shown are (a) P_{11}, (b) P_{13}, (c) P_{31}, and (d) P_{33}. The data-estimated propagators are computed using surface geophone 2 and the buried geophone at 1.05 m depth. Frequency filters are applied with a passband between 40 and 100 Hz.

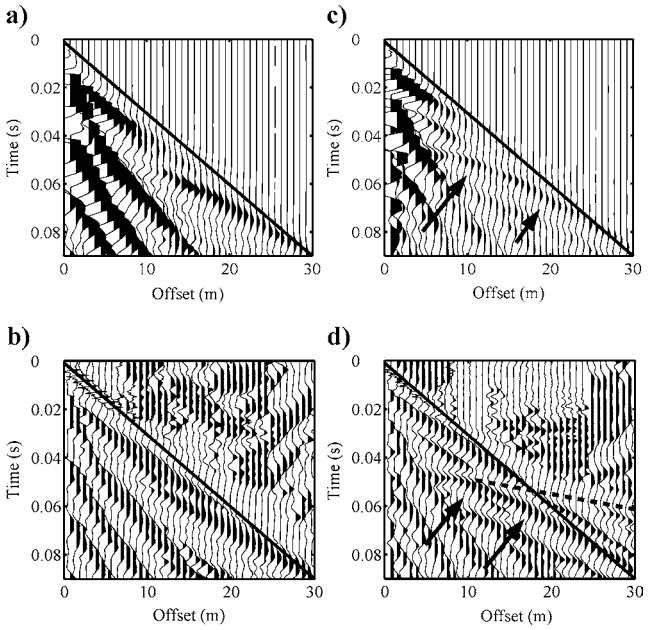

Figure 9. Near-source traces of walkaway noise survey for (a) v_x, (b) v_x with 0.005 s AGC window, (c) v_z, and (d) v_z with 0.005 s AGC window. The airwave is indicated by the solid line, the groundwater refraction by the dashed line, and the arrows indicate the reflected P-wave at the groundwater table.

indicates that the propagator inversion is robust in the presence of measurement errors.

DISCUSSION

Low near-surface velocities are obtained with PI, namely, $\alpha = 270 \pm 15$ m/s and $\beta = 150 \pm 9$ m/s using geophone 1. The Poisson's ratio σ that corresponds to these velocities is 0.28 with an uncertainty range between 0.18 and 0.34. Because the Poisson's ratio is sensitive to perturbations in the estimated velocities, it is difficult to make a sensible lithological interpretation. Despite this uncertainty, we may argue that the observed Poisson's ratio lies between the end-member models for dry, gas-saturated sands with $\sigma \in [0.0\ 0.22]$ and water-saturated sands with $\sigma \in [0.38\ 0.50]$ (Bourbié et al., 1987), which qualitatively makes sense because the considered sediment was partially water-saturated.

To test the results of PI, we analyzed the Zeist walkaway noise spread with recordings between 0- and 84-m offset. Near-offset sections of these data are shown in Figure 9. The receiver spacing is 0.75 m. No frequency filtering was applied to these multicomponent recordings. The airwave is clearly visible on both the inline and vertical components in the automatic gain control (AGC) plots. In the offset range between 0 and 10 m, we do not observe coherent energy arriving before the airwave. Events with a higher moveout velocity arrive just after the airwave. This indicates that the near-surface velocity is low, and that velocities increase with depth close to the free surface. Between 15- and 30-m offset, the refracted wave from the water table can be observed, and also the reflected wave from this interface can easily be identified on the vertical component. Thus, the near-offset section of the walkaway noise spread is qualitatively in agreement with the P-wave velocity obtained with PI for the very shallow near-surface.

In comparision to the results obtained with PI, we found a higher P-wave velocity with a dispersion analysis of guided waves. This difference can be attributed to the different depth sensitivity of dispersion analysis. Propagator inversion is only sensitive to wave velocities between the free surface and the buried geophone, whereas dispersion analysis is sensitive to velocities in the entire layer above the water table. For this reason, these low P- and S-wave velocities are not commonly observed in seismic surveys with a deeper target.

Although shallow material properties may influence the actual wave propagation, we believe that these have most impact on the measured wavefield. Both energy transmitted into the ground and recordings of the wavefield by geophones depend on the near-surface soil conditions. The repeatability of the source mostly depends on the (an)elastic properties of the soil (Aritman, 2001). Both the amount of energy radiated into the ground and the radiation pattern are influenced by the near-source material properties. Lateral variations in near-surface material properties could lead to poor repeatability of the source, degrading the quality of the seismic section. In addition, the measurements of the recording instruments differ from the actual ground motion. The so-called receiver coupling is influenced by the stiffness of the soil (Krohn, 1984). As a consequence, differences between recordings of adjacent receivers can exist as a result of coupling differences. Coupling errors especially affect the quality of converted-wave data. Thus, correct processing and interpretation of seismic data acquired in a land seismic survey require an understanding of both source and receiver coupling effects, and such an understanding may be facilitated by the very near-surface velocity estimates obtained using PI.

Another issue is the interaction of the wavefield with the free surface. Usually, we are only interested in the free-surface incident P- and S-waves, while receivers placed on land measure the interaction of these incident wavefields with the free surface. In principle, we can obtain the free-surface incident P- and S-waves using wavefield decomposition. Wavefield decomposition requires as input the free-surface reflectivity, which depends on the P- and S-wave velocities just below the free surface. Because we measure the wavefield exactly at the free surface, we should not use effective or averaged medium parameters for wavefield decomposition. Thus, the very shallow material properties obtained with PI may improve wavefield decomposition and demultiple methods.

Although application of the propagator method would require additional effort in acquiring data, we demonstrate that the technique provides additional information relevant for a land seismic survey. The propagator method can be incorporated into a seismic survey without having to perform an additional high-resolution experiment.

Finally, it should be mentioned that propagator estimation assumes that the medium is elastic. Although attenuation can be significant in the weathered layer, it does not affect the obtained results, since the dominant wavelength of the analyzed signal is not much smaller than the distance between the surface and the buried geophone.

CONCLUSIONS

The data-estimated propagator contains all information on the material parameters governing wave propagation between the free surface and the depth of a buried geophone. We applied PI on Zeist field data to determine the local near-surface velocities. This inversion yielded subsonic compressional wave velocity, $\alpha = 270 \pm 15$ m/s, and a low shear velocity, $\beta = 150 \pm 9$ m/s for the top meter.

Although very shallow anomalies are considered to have a small impact on the wavefield propagation, these may significantly influence the wavefield recordings. Both the energy transmitted into the subsurface by the source and receiver coupling depend on very shallow material properties. Hence, lateral changes in material properties could lead to poor repeatability of the source and receiver coupling differences. Also, corrections for the interaction of the wavefield with the free surface require these shallow wave velocities to be known.

ACKNOWLEDGMENTS

We thank Schlumberger for financially supporting this work. We further thank Henk van der Meer, Tim van Zon, and Stefan Carpentier for their help acquiring the field data, and Everhard Muyzert, Associate Editor J. Xia, and two anonymous reviewers for their constructive comments.

APPENDIX A

PROPAGATOR ESTIMATION USING WIENER DECONVOLUTION

In this section, we demonstrate the procedure to obtain the propagator filters, which are either symmetric or antisymmetric about $t = 0$, using Wiener deconvolution. We closely follow Yilmaz (2001) in our derivation, with the exception that we estimate acausal filters with symmetry conditions around t = 0.

Suppose that *f(t)* and *g(t)* are continuous signals, and that *h(t)* is given by the deconvolution of *f(t)* by *g(t)*:

$$h(t) = f(t) * g(t)^{-1}, \tag{A-1}$$

or, equivalently,

$$g(t) * h(t) = f(t), \tag{A-2}$$

where $*$ is the convolution operator. The function *h(t)* represents here the unknown propagator. Crosscorrelating equation A-2 with *g(t)* gives

$$R(t) * h(t) = q(t), \tag{A-3}$$

where $R(t)$ denotes the autocorrelation of $g(t)$ and

$$q(t) = \int_{-\infty}^{\infty} f(t+\tau) g(\tau) \mathrm{d}\tau. \tag{A-4}$$

Assume that we may approximate the propagator *h(t)* by a filter with $2M + 1$ independent coefficients. This reads, denoting the time series with a vector,

$$\mathbf{h} = [h_{-M}\ h_{-M+1} \ldots h_{-1}\ h_0\ h_1 \ldots h_{M-1}\ h_M]^T, \tag{A-5}$$

where ^{T} is the transpose operator. For a correlation with a maximum correlation length of $N + 1$, $\mathbf{q}$ has $2N + 1$ coefficients, and reads

$$\mathbf{q} = [q_{-N}\ q_{-N+1} \ldots q_{-1}\ q_0\ q_1 \ldots q_{N-1}\ q_N]^T. \tag{A-6}$$

Then, we may recast equation A-3 in a discrete form:

$$\mathbf{R}\mathbf{h} = \mathbf{q}. \tag{A-7}$$

The coefficients of the $(2N + 1) \times (2M + 1)$ autocorrelation matrix $\mathbf{R}$ are given by

$$R_{ij} = r_{|i-j|}, \tag{A-8}$$

where r_k denotes the kth lag of the autocorrelation of $\mathbf{g}$, and $N + 1$ is the maximum correlation length.

In order to take the symmetry conditions into account, we partition $\mathbf{q}$, $\mathbf{h}$, and $\mathbf{R}$:

$$\mathbf{h} = \begin{pmatrix} \mathbf{h}^- \\ \mathbf{h}^+ \end{pmatrix}, \qquad \mathbf{q} = \begin{pmatrix} \mathbf{q}^- \\ \mathbf{q}^+ \end{pmatrix}, \tag{A-9}$$

and

$$\mathbf{R} = \begin{pmatrix} \mathbf{R}^{-,-} & \mathbf{R}^{-,+} \\ \mathbf{R}^{+,-} & \mathbf{R}^{+,+} \end{pmatrix}. \tag{A-10}$$

The partitioned vectors are given by:

$$\mathbf{h}^- = [h_0/2\ \ h_{-1}\ \ h_{-2}\ \ \cdots\ \ h_{-M}]^T, \tag{A-11}$$

$$\mathbf{h}^+ = [h_0/2\ \ h_1\ \ h_2\ \ \cdots\ \ h_M]^T, \tag{A-12}$$

$$\mathbf{q}^- = [q_0\ \ q_{-1}\ \ q_{-2}\ \ \cdots\ \ q_{-N}]^T, \tag{A-13}$$

$$\mathbf{q}^+ = [q_0\ \ q_1\ \ q_2\ \ \cdots\ \ q_N]^T, \tag{A-14}$$

and the submatrices of $\mathbf{R}$ read as

$$\mathbf{R}^{+,+} = \mathbf{R}^{-,-} = \begin{pmatrix} r_0 & r_1 & r_2 & \ldots & & r_M \\ r_1 & r_0 & r_1 & \ddots & & r_{M-1} \\ r_2 & r_1 & r_0 & \ddots & & r_{M-2} \\ \vdots & \ddots & \ddots & \ddots & & \\ & & & & & r_1 \\ r_N & & & & r_1 & r_0 \end{pmatrix} \tag{A-15}$$

and

$$\mathbf{R}^{-,+} = \mathbf{R}^{+,-} = \begin{pmatrix} r_0 & r_1 & r_2 & \ldots & & r_M \\ r_1 & r_2 & r_3 & \ddots & & r_{M+1} \\ r_2 & r_3 & r_4 & \ddots & & r_{M+2} \\ \vdots & \ddots & \ddots & \ddots & & \\ & & & & & r_{M+N-1} \\ r_N & & & & r_{M+N-1} & r_{M+N} \end{pmatrix}. \tag{A-16}$$

Note that an additional row and column are added in the system of equations because the coefficients q_0 and $h_0/2$ appear both in the positive and negative parts of the partitioned vectors. It can be verified that equation A-7 can be rewritten in

partitioned form as

$$\begin{pmatrix} \mathbf{R}^{-,-} & \mathbf{R}^{-,+} \\ \mathbf{R}^{+,-} & \mathbf{R}^{+,+} \end{pmatrix} \begin{pmatrix} \mathbf{h}^{-} \\ \mathbf{h}^{+} \end{pmatrix} = \begin{pmatrix} \mathbf{q}^{-} \\ \mathbf{q}^{+} \end{pmatrix}. \tag{A-17}$$

For a symmetric filter, $\mathbf{h}^{-} = \mathbf{h}^{+}$, hence equation A-17 reduces to

$$(\mathbf{R}^{+,+} + \mathbf{R}^{+,-})\mathbf{h}^{+} = \frac{\mathbf{q}^{+} + \mathbf{q}^{-}}{2}, \tag{A-18}$$

whereas for an antisymmetric filter, $\mathbf{h}^{-} = -\mathbf{h}^{+}$. This gives

$$\left(\mathbf{R}^{+,+} - \mathbf{R}^{+,-}\right)\mathbf{h}^{+} = \frac{\mathbf{q}^{+} - \mathbf{q}^{-}}{2}. \tag{A-19}$$

These systems of equations can be solved for the independent filter coefficients using a damped least-squares solution. Prewhitening of the data is essential to avoid artifacts resulting from limited bandwidth.

REFERENCES

Aki, K., and P. G. Richards, 2002, Quantitative seismology, 2nd ed.: University Science Books.

Ammon, C. J., 1991, The isolation of receiver effects from teleseismic P waveforms: Bulletin of the Seismological Society of America, **81**, 2504–2510.

Aritman, B. C., 2001, Repeatability study of seismic source signatures: Geophysics, **66**, 1811–1817.

Bachrach, R., and A. M. Nur, 1998, High-resolution shallow-seismic experiments in sand, Part I: Water table, fluid flow, and saturation: Geophysics, **63**, 1225–1233.

Bachrach, R., J. Dvorkin, and A. M. Nur, 1998, High-resolution shallow-seismic experiments in sand, Part II: Velocities in shallow unconsolidated sand: Geophysics, **63**, 1234–1240.

Baker, G. S., D. W. Steeples, and C. Schmeissner, 1999, In-situ, high-resolution P-wave velocity measurements within 1 m of the earth's surface: Geophysics, **64**, 323–325.

Birkelo, B. A., D. W. Steeples, R. D. Miller, and M. Sophocleous, 1987, Seismic reflection study of a shallow aquifer during a pumping test: Ground Water, **25**, 703–709.

Bourbié, T., O. Coussy, and B. Zinszner, 1987, Acoustics of porous media: Technip.

Curtis, A., and J. O. A. Robertsson, 2002, Volumetric wavefield recording and wave equation inversion for near-surface material properties: Geophysics, **67**, 1602–1611.

Dankbaar, J. W. M., 1985, Separation of P- and S-waves: Geophysical Prospecting, **33**, 970–986.

Doornenbal, J. C., and K. Helbig, 1983, High-resolution seismics on a tidal flat in the Dutch Delta — Acquisition, processing and interpretation: First Break, **1**, 9–20.

Gilbert, F., and G. E. Backus, 1965, Propagator matrices in elastic wave and vibration problems: Geophysics, **31**, 326–332.

Goforth, T., and C. Hayward, 1992, Seismic reflection investigations of a bedrock surface buried under alluvium: Geophysics, **57**, 1217–1227.

Haskell, N., 1953, The dispersion of surface waves in multilayered media: Bulletin of the Seismological Society of America, **43**, 17–34.

Helmberger, D., and R. A. Wiggins, 1971, Upper mantle structure of Midwestern United States: Journal of Geophysical Research, **76**, 3229–3245.

Hunter, J. A., S. E. Pullan, R. A. Burns, R. M. Gagne, and R. L. Good, 1984, Shallow seismic reflection mapping of the overburden bedrock interface with the engineering seismograph — Some simple techniques: Geophysics, **49**, 1381–1385.

Kähler, S., and R. Meissner, 1983, Radiation and receiver pattern of shear and compressional waves as a function of Poisson's ratio: Geophysical Prospecting, **31**, 421–435.

Krohn, C. E., 1984, Geophone ground coupling: Geophysics, **49**, 722–731.

Michaels, P., 2002, Identification of subsonic P-waves: Geophysics, **67**, 909–920.

Muijs, R., K. Holliger, and J. O. A. Robertsson, 2002, Perturbation analysis of an explicit wavefield separation scheme for P- and S-waves: Geophysics, **67**, 1972–1982.

Robertsson, J. O. A., and A. Curtis, 2002, Wavefield separation using densely deployed three–component single–sensor groups in land surface–seismic recordings: Geophysics, **67**, 1624–1633.

Robertsson, J. O. A., K. Holliger, A. G. Green, A. Pugin, and R. D. Iaco, 1996, Effects of near-surface wave guides on shallow high-resolution seismic refraction and reflection data: Geophysical Research Letters, **23**, 495–498.

Steeples, D. W., and R. D. Miller, 1990, Seismic reflection methods applied to engineering, environmental and groundwater problems, *in* S. H. Ward, ed., Geotechnical and environmental geophysics I: SEG, 1–30.

Stümpel, H., S. Kähler, R. Meissner, and B. Milkereit, 1984, The use of seismic shear waves and compressional waves for lithological problems of shallow sediments: Geophysical Prospecting, **32**, 662–675.

Thomson, W. T., 1950, Transmission of elastic waves through a stratified solid medium: Journal of Applied Physics, **21**, 89–93.

Trampert, J., M. Cara, and M. Frogneux, 1993, SH propagator matrix and Q_S estimates from borehole- and surface-recorded earthquake data: Geophysical Journal International, **112**, 290–299.

Van Vossen, R., J. Trampert, and A. Curtis, 2004, Propagator and wave-equation inversion for near-receiver material properties: Geophysical Journal International, **157**, 796–812.

Verschuur, D. J., A. J. Berkhout, and C. P. A. Wapenaar, 1992, Adaptive surface-related multiple elimination: Geophysics, **57**, 1166–1177.

Wapenaar, C. P. A., P. Herrmann, D. J. Verschuur, and A. J. Berkhout, 1990, Decomposition of multicomponent seismic data into primary P- and S-wave responses: Geophysical Prospecting, **38**, 633–661.

Ward, S. H., 1990, Geotechnical and environmental geophysics, vol. I–III: SEG.

Yilmaz, O., 2001, Seismic data analysis I — Processing, inversion and interpretation of seismic data: SEG.